Chinese Chemical Letters 37 (2026) 111370

Contents lists available at ScienceDirect

Chinese Chemical Letters

journal homepage: www.elsevier.com/locate/cclet

Synergistic Co Pd affection impart high overall water splitting efficiency to Pt/Ir-based electrocatalyst in acid

Zicong Yang[a], Guangshun Ran[a,b], Hui Song[a], Yukun Chang[a], Jinshu Wang[a], Hongyi Li[a,c,*]

[a] State Key Laboratory of Materials Low-Carbon Recycling, College of Material Science and Engineering, Beijing University of Technology, Beijing 100124, China
[b] Institute of High Energy Physics, Chinese Academy of Sciences, Beijing 100049, China
[c] College of Carbon Neutrality Future Technology, Beijing University of Technology, Beijing 100124, China

ARTICLE INFO

Article history:
Received 19 December 2024
Revised 14 May 2025
Accepted 24 May 2025
Available online 25 May 2025

Keywords:
Water splitting
Noble metal
Hydrogen evolution reaction
Oxygen evolution reaction
MXene

ABSTRACT

To enhance the suitability of noble metal-based electrocatalysts for acidic overall water splitting, a Pt/Ir-based electrocatalyst incorporating Co and Pd anchored on $Ti_3C_2T_x$ MXene (Ir/Co Pt Pd@MX) has been successfully synthesized. The incorporation of Co during the synthesis process increases the valence states of Ir and Pt, resulting in improved electrocatalytic performance. The Ir/Co Pt Pd@MX exhibits a low HER overpotential of 38 mV and an OER overpotential of 230 mV, outperforming commercial catalysts. The low noble metal containing electrocatalyst shows nearly 10 times the mass activity of Pt/C for HER and 35 times that of Ir/C for OER. The water splitting cell voltage is 1.46 V, with no observable decay after a 24-h stability test at 10 mA/cm^2, establishing it as a top-tier noble metal-based electrocatalyst in acidic environments. Density functional theory (DFT) calculations indicate that Co facilitates the deposition of Ir, enhancing OER performance, while Pd restrict H^+absorption of Ir, ensuring the stability. The energy barrier of the rate-determining steps for both the HER and OER decreases.

© 2025 Published by Elsevier B.V. on behalf of Chinese Chemical Society and Institute of Materia Medica, Chinese Academy of Medical Sciences.

Electrocatalytic water splitting is known as a proper access to hydrogen energy which include hydrogen evolution reaction (HER) and oxygen evolution reaction (OER) [1–3]. As for acidic water splitting, which is critical for polymer membrane electrolyzer, presents a series of advantages including high gas purity and proton conductivity along with little gas crossover [4,5]. HER in acidic electrolyte with abundant H^+ is obviously the suitable method with maximum efficiency. However, in acidic condition, OER is severely affected by high concentration of H^+ while the transition from H_2O to O^* need more energy compared to OH^- to O^* in alkaline electrolyte. With this being noticed, an overall water splitting electrocatalyst design which is suitable in acidic environment is crucial.

The platinum is undoubtedly the best electrocatalyst among all for HER, which is illustrated by the Gibbs free energy volcano where platinum (Pt) is on top. As for OER, iridium (Ir) and ruthenium (Ru) are ideal choices [6–9]. However, as for water splitting, high reaction potential in acidic condition would cause degradation of electrocatalyst especially for Ru [4], the soluble RuO_4 would appear due to the overoxidation. In this case, Ir seems to be a proper candidate for OER during acidic water splitting. The degradation of Ir to IrO_4^{2-} can also happen during long time reaction [10]. So the Ir should be “protected”. Wang *et al.* use carbon nanotube as a protector of IrCo nanoparticles to achieve high efficiency and good stability [11]. The “shield” scheme is a direct way of protection but it also hinders the direct contact between electrolyte and electrocatalyst, which could affect the catalytic efficiency.

The underlying mechanism behind degradation in acidic electrolyte is primarily due to the absorption of H^+ ions. Within the water electrocatalysis, Pt is expected to serve as a hydrogen ion (H^+) acceptor during the HER process, whereas Ir should remain unaffected by H^+ ions to prevent any compromise in catalytic efficiency due to dysfunctionality in OER [12]. To prevent Ir from potential poisoning by H^+, palladium (Pd) emerges as a promising candidate capable of fulfilling the role of a proton acceptor. Palladium and its oxide known for their affinity for hydrogen as well as rather good electrocatalysis activity seem to be promising for protect to Ir from H^+. Pd is more abundant than Pt on earth alongside with superior electrochemical activity [5]. Utilizing a catalyst with "H acceptor" for Ir-containing materials may represent a viable approach for strategically modulating the electronic configuration of the catalytically active sites for OER. A catalyst with Pd as guarantee for HER as well as “H^+acceptor” for Ir from degra-

* Corresponding author.
E-mail address: lhy06@bjut.edu.cn (H. Li).

https://doi.org/10.1016/j.cclet.2025.111370
1001-8417/© 2025 Published by Elsevier B.V. on behalf of Chinese Chemical Society and Institute of Materia Medica, Chinese Academy of Medical Sciences.

dation in acidic environment could be an ideal select for overall water splitting candidate. Furthermore, considering the low storage of iridium on earth, the amount of Ir usage is also crucial [13,14].

In this case for the noble metal introduction, cobalt (Co) could act as an assistance [15,16]. Chang *et al.* studied the mechanism of the function of Co in PtCo alloy [17]. Co lowers energy barrier for Pt deposition. As is known, Ir owns similar electronic configuration as Pt with 5d and 6 s orbitals being relatable to their chemical behavior. So the potential of Co utilization in Ir and Pt introduction is worth exploring [11,16,18].

MXenes known as novel 2D material firstly reported in 2011 [19] have become a gigantic family containing multiple transition metal carbide/nitride [20–22], which means their roles in electrocatalysis still need to be further explored. The 2D morphology and good conductivity along with excellent mechanical properties make MXenes outstanding substrate for electrocatalyst [23–25], batteries [26] and supercapacitor [27,28].

According to the above, an electrocatalyst capable for overall water electrocatalysis in acidic electrolyte incorporating Co-assisted oxides of Pt, Ir, Pd nanoparticles immobilized onto ultrathin $Ti_3C_2T_x$ MXene, has been synthesized. According to density functional theory (DFT) calculation, the cobalt plays a vital role in facilitating the noble metal deposition and nucleation. Furthermore, the addition of Co increases the valence state of Ir and Pt, which could elevate the electrocatalysis activity. Pt and Pd act as HER active sites as well as H acceptor which significantly decrease the absorption effect of Ir. Meanwhile, Ir serves as OER active sites, safeguarded by the presence of Pd, thereby enhancing the stability. The MXene substrate offers abundant nucleation sites for noble metal oxide owing to its high specific surface area with rich surface functional groups. The electrocatalyst shows a rather low overall water splitting potential of 1.46 V at 10 mA/cm^2 and remains unchanged in potential after 28 h stability test at 10 mA/cm^2. The electrochemical performances make it superior electrocatalyst in acidic overall water splitting and offers a new strategy in modifying noble metal electrocatalyst.

As for the preparation of noble metal composite, the ultrathin MXene is synthesized according to our previous work [29]. 2 g Ti_3AlC_2 MAX powder (500 mesh) is submerged in 20 mL 6 mol/L KOH for 96 h. Subsequently, the mixture is rinsed with deionized water (DI water) and dissolved into 20 mL hydrochloric acid for 24 h. The resultant undergoes several washes and neutralization with DI water before being collected via centrifugation. Upon the pH approaching 7, the slurry is ultrasonically dispersed in 50 mL DI water and freeze-drying for 3 days. The resulting product is designated as ultrathin MXene. 100 mg ultrathin MXene are dispersed ultrasonically in 30 ml ethylene glycol for 30 min, denoted as solution A. Solution A is then heated in an oil bath to 180 °C. Meanwhile, 36 mg cobalt nitrate is dissolved in 4 mL of 5 mg/mL chloroiridic acid. The aforementioned solution is drop-casted in solution A while maintaining a temperature of 180 °C. The resulting mixture is heated for 1 h. Subsequently, 20 mg sodium tetrachloropalladium is added, followed by additional 1-h heating period. 10 mg of chloroplatinic acid is introduced and allowed to react for another 30 min oil bath. The final solution is cooled down to room temperature and washed with methanol for 4 times before being collected *via* centrifugation. The resulting catalyst is obtained through vacuum drying at 60 °C for 12 h and is named as Ir/Co Pt Pd @MX". Based on the procedure above, "Ir Pt@MX", "Ir/Co Pt@MX" and "Ir/Co Pt Pd" are successfully synthesized without correspond metal ion or MXene. 40 wt% Pt/C and 20 wt% Ir/C commercial catalyst are used for comparison.

Fig. 1a illustrates the schematic representation of the synthesis pathway for Ir/Co Pt Pd@MX. The ultrathin MXene was produced through a successful process involving KOH and *in-situ* HF etching. The ultrathin MXene facilitates numerous nucleation sites, which are subsequently subjected to a heated glycol solution containing various metal ion salts at 180 °C. The presence of glycol plays a crucial role in preventing the oxidation of Ti-based MXene to TiO_2, a transformation that could significantly interfere the electrochemical performance of the electrocatalysts. Finally, Ir/Co Pt Pd@MX was successfully synthesized.

The X-ray Diffraction (XRD) patterns depicting the synthesized catalysts are presented in Fig. 1b. Upon incorporation of noble metals, different characteristic peaks emerge, PtO (PDF #43–1100) at 33.581°, IrO_2 (PDF #43–1019) at 28.027°, and PdO (PDF #43–1024) at 33.889°. It is noteworthy that the absence of IrO_2 peaks in the Ir/Co Pt Pd@MX curve can be attributed to the minimal noble metal content (7 $\mu g_{Ir}/mg_{catalyst}$ according to ICP result) as well as other noble-metals (13 $\mu g_{Pt}/mg_{catalyst}$ and 7 $\mu g_{Pd}/mg_{catalyst}$). The scarcity presence of noble-metal oxides may be obscured by the intense peaks of the $Ti_3C_2T_x$ MXene substrate. Regarding the MXene substate, the pristine ultrathin MXene XRD spectra reveals an intense prominent peak at 6.998° represent (002) crystal interface which is also the characteristic peak of $Ti_3C_2T_x$ MXene. The feature is evident in the magnified region of 5°−10° of the XRD patterns in Fig. 1a. With Ir and Pt introduced, a shift to a smaller angle occurs, from 6.998° to 6.287°, indicating the successful introduction. Furthermore, with additional elemental additions, the peaks progressively shift to smaller positions, reaching 6.121° and 5.731°, thereby affirming successful element integration. Fig. 1c illustrates the morphology of ultrathin MXene sheets, showcasing evident surface wrinkles that offer abundant active sites for nucleation. Fig. S1 (Supporting information) shows intuitively about the noble-metal electrocatalyst anchoring on the surface of MXenes. The line scan analysis of nanoparticles in Fig. 1d reveals their elemental composition, where the high intensity of Ti Kα1 indicates the predominance of Ti in the MXene substrate, while the descending curves corresponding to Pt, Pd, and Ir curves confirm the presence of noble metals. Fig. 1e presents elemental mapping, indicating uniform distribution of these noble metal elements over a rather larger area. Since the morphology of the electrocatalyst is nanoparticle in conjunction with 2D material, the N_2 absorption-desorption tests shown in Fig. 1f were conducted. Intriguingly, the addition of Co leads to an increase in specific surface area from 3.780 m^2/g to 5.031 m^2/g. Furthermore, with cooperation of Pd, the specific surface area further escalates to 8.175 m^2/g. Analysis of pore size distribution illustrated in Fig. S2 (Supporting information) indicates that the augmentation in specific surface area primarily stems from an increase in mesopores. This underscores the role of Co and Pd in facilitating the formation of mesopores in Ir/Pt-containing samples.

For a detailed examination of the electrocatalyst nanoparticles composed of MXene, the transmission electron microscope (TEM) image in Fig. 1g is presented. It illustrates the composite structure of MXene and the electrocatalyst, with nanoparticles prominently attached to the MXene surface. Upon closer inspection at higher magnification, a greater number of nanoparticles are observed besides those visible nano-clusters shown in the scanning electron microscope (SEM) image. Fig. 1h provides an enlarged view of the region depicted in Fig. 1g to facilitate statistical analysis. The particle size distribution, as depicted in the inset, clearly shows Ir/Co Pt Pd@MX nanoparticles with an average size of 2.022 ± 0.02 nm. This ultra-small particle size enhances the interaction between the electrocatalyst and the electrolyte and increases the proportion of metal oxides since the noble metal are easily to be oxidized at the surface of a nanoparticle [30], thereby improving electrocatalytic performance. In addition to the particle size, elemental distribution is characterized by high-angle annular dark-field (HAADF) mapping, as shown in Fig. S3 (Supporting information). The presence

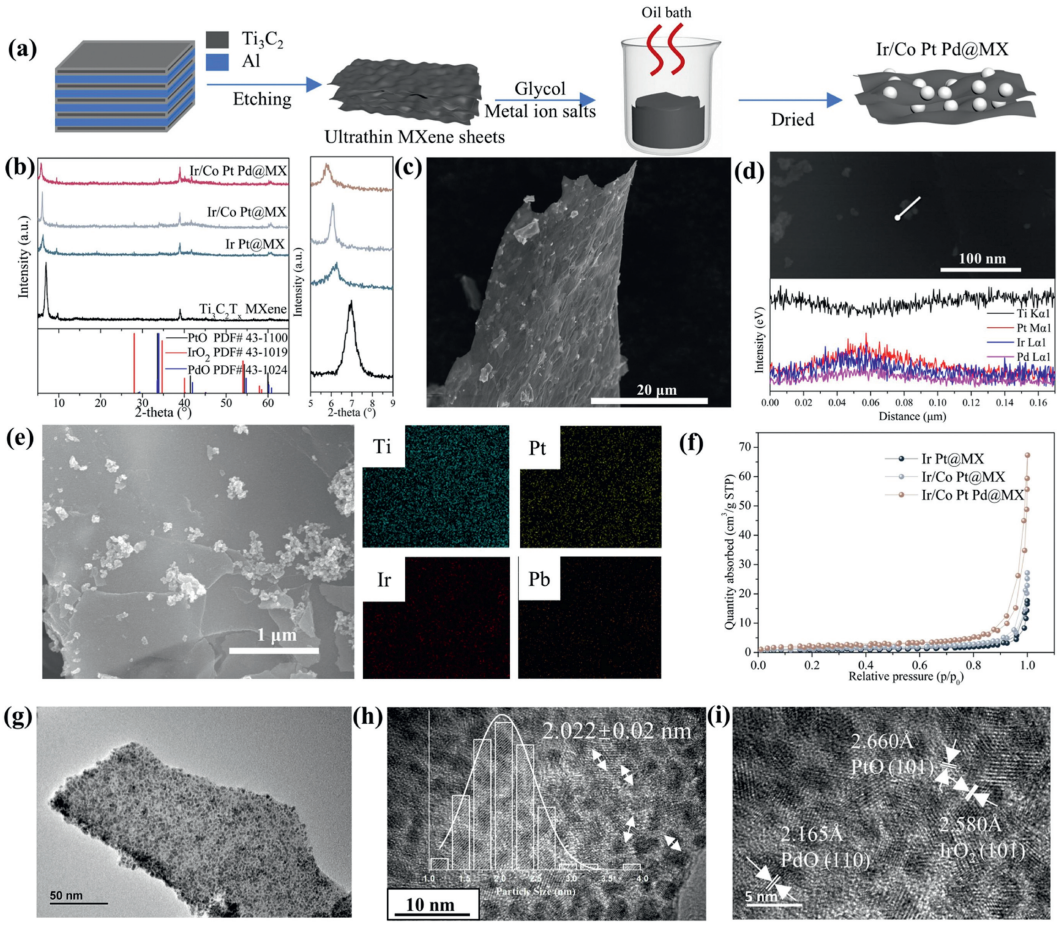


Fig. 1. (a) Schematic diagram of the synthesis route of Ir/Co Pt Pd@MX. (b) XRD patterns of electrocatalysts and $Ti_3C_2T_x$ MXene. (c) SEM image of ultrathin MXene sheet. (d) Line scan of single Ir/Co Pt Pd@MX particle. (e) SEM image of Ir/Co Pt Pd@MX and corresponding EDS mapping of Ti, Pt, Ir, Pd. (f) N_2 absorption-desorption curves of all the electrocatalysts. (g) TEM image of Ir/Co Pt Pd@MX. (h) Particle size investigation of Ir/Co Pt Pd@MX with particle size distribution in the inset. (i) HRTEM of Ir/Co Pt Pd@MX with crystal interplanar spacing marked.

of titanium in significant quantities confirms the existence of the MXene sheet, while the uniformly distributed cobalt underscores its crucial role in the synthesis process. The noble metals are concentrated not only within nano-clustered areas but also distributed across the MXene surface, proving the elemental composition of the nanoparticles observed in the TEM image.

High-resolution transmission electron microscopy (HRTEM) in Fig. 1i visually confirms the successful incorporation of noble metals. Measurements of interplanar spacing reveal specific crystal planes of noble metal oxides. In the small area examined, interplanar spacings of 2.165 Å corresponding to PdO (110), 2.580 Å to IrO_2 (101), and 2.660 Å to PtO (101) are observed. Furthermore, the presence of PtO in this electrocatalyst guarantees improved hydrogen evolution reaction (HER) performance.

To take a deeper look inside the valence changing and oxidation state brought by element introduction. X-ray photoelectron spectroscopy (XPS) tests were conducted, as illustrated in Figs. 2a-c. It is evident that all the noble metals are reduced to metal forms or oxide forms because of reduction effect of glycol at high temperature [31]. As shown in Fig. 2a, the Ir 4f doublets shift to higher binding energies, from 60.76 eV to 61.94 eV, upon the introduction of cobalt and palladium. This shift indicates that iridium transitions to a higher oxidation state [15]. For the Ir Pt@MX, the iridium shows in Ir^{2+} and Ir^{4+} while after the addition of Co [32], the Ir^{4+} peaks appear, which is more beneficial for OER since high oxidation state Ir owns high activity in OER process due to previous reported DFT calculation [33,34]. Additionally, a higher valence state of iridium enhances resistance to "poisoning" by abundant H^+in acidic environments, thereby improving stability during the water-splitting process. Same phenomenon can be seen in Pt 4f XPS spectra in Fig. 2b, where the Pt valence turned higher with addition of Co and Pd. Most importantly, the proportion of Pt^{2+} gets larger with the overall valence increasement. Eventually, The Pt^{2+} characteristic peak at 72.4 eV is perfectly meet the spectra of Ir/Co Pt Pd@MX [35]. Besides, as the introduction of Co, there show another doublet located at 73 eV which are higher than Pt^{2+} but lower than Pt^{4+}.The PtO specie, which are rich in oxygen vacancies and defects, can act as active sites for HER during H^+ reduction process. Moreover, the intermediate valence state of PtO, being lower than PtO_2 and higher than metallic Pt, achieves an optimal balance in the absorption and desorption processes of *H. As the valences of Ir and Pt increase, the Co shows a majority of low valence of Co^{2+} in Fig. 2c. Fig. S4 (Supporting information) presents the Pd 3d spectra, which shows the existence of PbO. The XPS spectra of noble metals in Ir/Co Pt Pd@MX are consistent with the crystal lattice observed in HRTEM. Besides, by the analyzation of XPS survey spectra in Fig. S5 (Supporting information), it is worth noting that the F 1s and F auger KL1 peaks diminish as the introduction of Co and Pd. This suggests that cobalt facilitates the incorporation of noble metals, resulting in the occupation of fluorine sites, which are prevalent in Ir Pt@MX, almost disappearing in Ir/Co Pt Pd@MX. Since the fluorine groups can significantly impede electrocatalysis

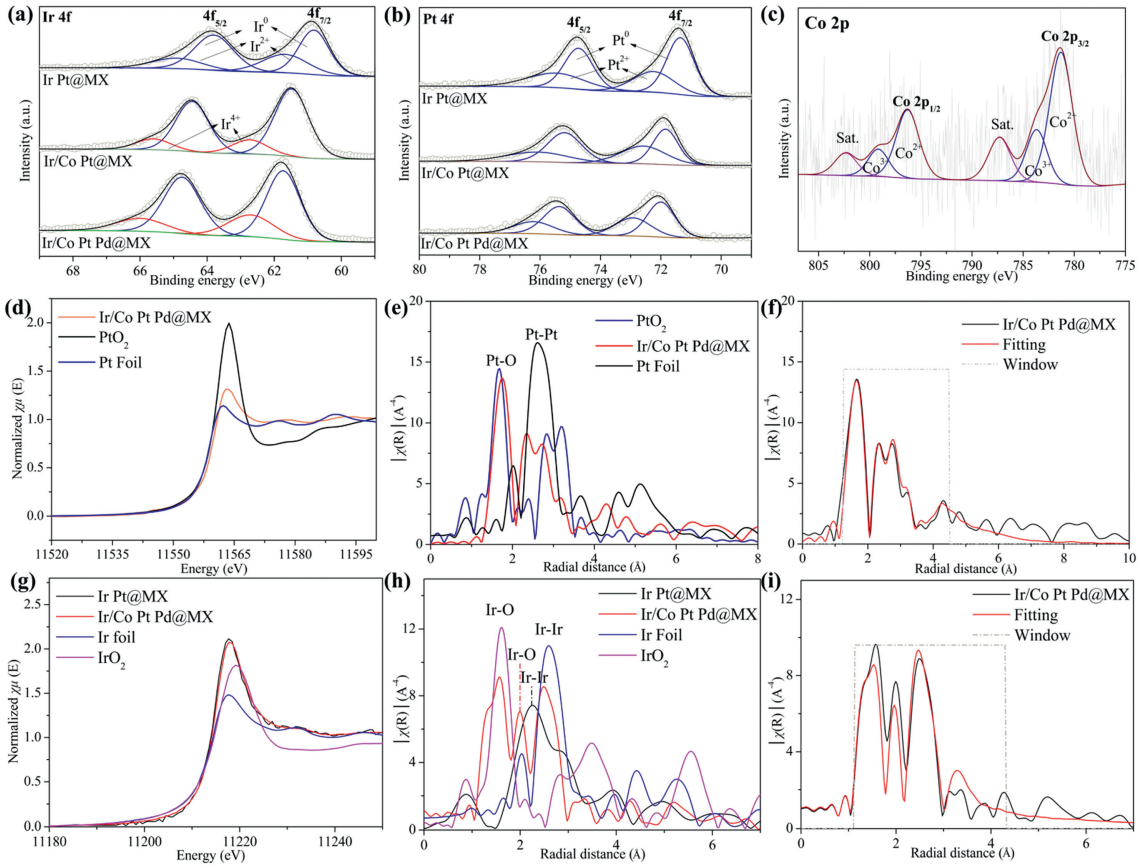


Fig. 2. XPS spectra of (a) Ir 4f, (b) Pt 4f of Ir Pt@MX, Ir/Co Pt@MX and Ir/Co Pt Pd@MX. (c) XPS spectra of Co 2p of Ir/Co Pt Pd@MX. (d) Normalized XANES spectra of Pt L3-edge Ir/Co Pt Pd@MX and reference samples, (e) Pt L3-edge Fourier-transfer (FT) EXAFS spectra of the Pt element of Ir/Co Pt Pd@MX and reference samples. (f) FT-EXAFS fitting curves of Ir/Co Pt Pd@MX (reference: Pt3O4). (g) Normalized XANES spectra of Ir L3-edge Ir Pt@MX, Ir/Co Pt Pd@MX and reference samples, (h) Ir L3-edge FT-EXAFS spectra of the Ir element of Ir Pt@MX, Ir/Co Pt Pd@MX and reference samples. (i) FT-EXAFS fitting curves of Ir/Co Pt Pd@MX (reference: IrO_2).

[36,37], the Ir/Co Pt Pd@MX is expected to outperform Ir Pt@MX in electrochemical tests.

The XAFS test shown in Figs. 2d-i further reveal the Pt/Ir state of Ir/Co Pt Pd@MX. The normalized L_3-edge of Pt depicted in Fig. 2d evidently show the oxidation state of Pt in Ir/Co Pt Pd@MX. The white line (WL) intensity of Ir/Co Pt Pd@MX located in the middle of Pt foil and PtO_2 references, suggesting the oxidation state of Pt element in the catalyst is intermediate between +4 and 0. Besides, the absorption edge of Ir/Co Pt Pd@MX clearly shifts to a higher energy, indicative of a lower electron density [38], which implies that the Ir/Co Pt Pd@MX is easier to accept e^- to complete the process of H^+ reduction. Fig. S6 (Supporting information) shows the full post-edge of Ir/Co Pt Pd@MX, comparing with PtO_2 and Pt foil, the wave shape of Ir/Co Pt Pd@MX is similar to Pt foil, which means the Ir/Co Pt Pd@MX still owns metallic properties. For a detailed analysis of the bonding type, a Fourier-transforms (FT) of L_3-edge extended X-ray absorption fine structure (EXAFS) based on K oscillation function in Fig. S7 (Supporting information) is shown in Fig. 2e. By comparing with reference samples of Pt-foil and PtO_2 whose fitting curves perfectly meet the corresponding theoretical FT-EXAFS reference shown in Fig. S8 (Supporting information), which indicates a prevalent Pt-O bond in Ir/Co Pt Pd@MX with a reduced presence of Pt-Pt bonding. To further investigate the Pt bonding types, an instantaneous fitting was conducted. As illustrated in Fig. 2f, the FT-EXAFS spectra of the L_3-edge of Pt in Ir/Co Pt Pd@MX align perfectly with the curves of Pt_3O_4, achieving an R-factor of 0.0016. This finding corroborates the valence states observed in the XPS spectra. Furthermore, according to the oxidation state calculation of Pt in conjunction with the k-edge absorption energy, the ~2.6 valence of Pt meets the fitting result of FT-EXAFS.

To thoroughly examine the impact of cobalt introduction on the iridium site, Fig. 2g shows the normalized XANES spectra of Ir L_3-edge of Ir/Co Pt Pd@MX and reference samples. The primary peaks of both Ir Pt@MX and Ir/Co Pt Pd@MX positioned between Ir foil and IrO_2 references, which is consistent with the XPS valence state analysis. The WL intensity indicate the unoccupied state in 5d band, which correlates to the electronic structure and catalytic behavior [39]. When comparing Ir Pt@MX with Ir/Co Pt Pd@MX, the absorption edge of Ir/Co Pt Pd@MX shift to a higher energy state, indicating the Ir in Ir/Co Pt Pd@MX owns higher oxidation state than non-cobalt containing electrocatalyst. This suggests that Co increases the oxidation state of Ir during the synthesis process, thereby enhancing the activity of the Ir site in the OER. The post-edge in Fig. S9 (Supporting information) also shows metallic properties, ensuring overall stability in electrocatalysis. The FT-EXAFS L_3-edge curves in Fig. 2h displays the bonding difference due to the presence of Co. Compared to the reference samples of Ir foil and IrO_2, which are accurately fitted as shown in Fig. S10 (Supporting information), the peak of Ir/Co Pt Pd@MX aligns with the Ir-O peak of IrO_2, whereas the sample without cobalt shows a peak corresponding to Ir-Ir as seen in the Ir foil. Additionally, Ir/Co Pt Pd@MX exhibits a peak for Ir-Ir at approximately 2.53 Å, suggesting the coexistence of both IrO_2 and metallic Ir. Fig. 2i intuitively display the fitting curves of FT-EXAFS of Ir/Co Pt Pd@MX based on EXAFS Ir L_3-edge oscillation function in Fig. S11 (Support-

ing information). The Ir/Co Pt Pd@MX sample partially matches the theoretical FT-EXAFS curves of IrO_2. Since the sample itself is not pure IrO_2 through XPS investigation, the slightly shifted peak further proves the conclusion. In contrast, the non-cobalt containing sample, Ir Pt@MX, shows a composition of pure Ir as illustrated in Fig. S12 (Supporting information), where the Ir L_3-edge EXAFS and FT-EXAFS exhibit clear consistency between Ir Pt@MX and metallic Ir, achieving an R-factor of 0.08. These analyses highlight the influence of cobalt introduction at Ir sites. The alterations in bonding type and oxidation state synergistically enhance the activity of Ir active sites in overall water splitting electrocatalysis.

To investigate the critical electrochemical performance, a preliminary study was conducted on the impact of Co on Ir during the OER under alkaline conditions. As depicted in Fig. S13 (Supporting information), the Ir@MX exhibits a significantly higher double-layer capacitance (4.2 mF/dec) compared to Co@MX (0.8 mF/dec), attributable to its noble metal properties. Based on the equation mentioned in supplementary, the electrochemical active surface area (ECSA) is easily to be calculated as (105 cm^2/mg), which is more than five times greater than that of Co@MX (20 cm^2/mg). Intriguingly, upon incorporation of Co with Ir, the C_{dl} sharply increases to 18.07 mF/dec. This observation is further supported by the LSV curves for OER under alkaline conditions, as presented in Fig. S14, where Ir/Co@MX demonstrates superior OER performance. This test in alkaline electrolyte highlights the Co affection in Ir. Since the Co itself did not show stupendous OER activity, it enhances the performance of Ir as the primary active site, thereby delivering exceptional electrochemical performance.

With this prerequisite, a similar C_{dl} test in acidic electrolyte of Ir Pt@MX, Ir/Co Pt Pd@MX and Ir/Co Pt Pd is performed. As Fig. 3a illustrated, predictably, the introduction of Co resulted in higher C_{dl} values in both electrolytes compared to non-cobalt one. With the inclusion of MXene, the C_{dl} of Ir/Co Pt Pd increased from 6.54 mF/dec to 10.49 mF/dec, indicating an enriched ECSA. This highlights the significant role of MXene in enhancing electrochemical performance. To reveal the role MXene plays, the electronic impedance spectra (EIS) is shown in Fig. S14 (Supporting information) along with an equivalent circuit in the inset. Unlike the C_{dl} result, the MXene plays a decisive role in altering charge transfer resistance (R_{ct}) changing. As Fig. S15 (Supporting information) illustrated, all three electrolyte shows similar solution resistance at around 1 Ω due to their identical eletrolyte. Nevertheless, with MXene cooperated, the R_{ct} of Ir Pt@MX (0.74 Ω) and Ir/Co Pt Pd@MX (0.39 Ω) are much lower than the one without MXene. Even though the R_{ct} of Ir/Co Pt Pd is still not rather high in value (6.8 Ω), the MXene still decrease the R_{ct} by an order of magnitude. To show what a difference can a composite of 2D material with high conductivity and nanoparticles with high ECSA make, a series of LSV test is performed.

Fig. 3b shows the LSV curves of HER. The Ir Pt@MX shows an overpotential of −92 mV at −10 mA/cm, This sample contains a noble metal content of 14 μg, consisting of both Pt and iridium Ir. These results suggest that the simple mere addition of a small amount of Pt does not significantly enhance the HER performance. However, with the introduction of Co and Pd, the overpotential decreases to 48 mV. This improvement can be attributed to the incorporation of Co, which increases the oxidation state of Pt, and the role of Pd in H^+ absorption. The overpotential for the Ir/Co Pt Pd nanoparticle is already comparable to that of commercial Pt/C. When combined with the synergistic effects of MXene as a substrate, the overpotential further decreases to 37 mV. Fig. 3c investigate the kinetics of all these samples by Tafel slope calculation. The HER goes in acidic solution associated with both absorption and desorption of hydrogen intermediate (H^*). The Tafel slope analysis provides insights into the rate-determining step of the reaction [53,54]. The Ir Pt@MX shows a relatively large Tafel slope of 151 mV/dec which means the rate-determining step is Volmer reaction:

$$H^+ + e^- \rightarrow H^*$$

While other electrocatalysts show a Tafel slope in between 40 mV/dec and 120 mV/dec, which shows a Volmer-Heyrovsky step with a rate-determining step of Heyrovsky reaction [55]:

$$H^* + H^+ + e^- \rightarrow H_2$$

However, the Ir/Co Pt Pd@MX shows a minimum Tafel slope among all the references with 25.1 mV, which means the mechanism of Ir/Co Pt Pd@MX is different from other references. The Volmer-Tafel step is the main reaction and the rate-determining step has changed to Tafel reaction:

$$2H^* \rightarrow H_2$$

Since the Pd introduction increase the ability in H^+ absorption along with MXene improving conductivity. The Ir/Co Pt Pd@MX shows the best HER performance among all the samples.

Fig. 3d exhibits the LSV curves of OER of corresponding electrocatalysts. As is shown, the overpotential at 10 mA/cm^2 of Ir Pt@MX is 480 mV, indicating a poor OER properties due to the little Ir contain. In comparison, the 20 % Ir/C catalyst shows an overpotential of 385 mV. Although the commercial catalyst has a sufficiently low onset potential, its intrinsic OER activity limits its overall performance. With Co and Pd introduction, the overpotential finally decreases to 200 mV for Ir/Co Pt Pd@MX. It is worth noting that the LSV curves of Ir/Co Pt@MX shows abnormal shape where the two peaks appeared. This is due to the remaining Co dissolution under acidic condition without the protection of Pd. For the one with Pd protection, the H^+ in electrolyte partially absorbed by Pd, thereby limiting Co corrosion. For the Ir/Co Pt Pd nanoparticles, it shows a good overpotential of 330 mV. The addition of MXene sheets further enhances the OER performance by improving the conductivity. When the kinetics of OER is taken into consideration in Fig. 3e, the Ir/Co Pt Pd@MX shows a low Tafel slope of 74.4 mV/dec, which outperforms the one without Co Pd introduction (324.9 mV/dec) and commercial 20 % Ir/C electrocatalyst (156.8 mV/dec). This indicates a dramatic improvement in intrinsic catalytic activity [38,53].

Fig. 3f provides the bar chart of overpotentials of corresponding samples. Notably, the Ir/Co Pt Pd@MX exhibits the lowest overpotential for both HER and OER. To evaluate the enhancement in mass activity normalized to 1 mg of noble metal, a bar chart of mass activity is shown in Fig. 3g The noble metal content (Pt, Ir, Pd) was quantified using inductively coupled plasma optical emission spectrometry (ICP-OES). The Pt/C and Ir/C were considered as 25 μg and 100 μg respectively to match the actual usage in commercial scale. The Ir/Co Pt Pd@MX shows a high mass activity of 7.75 A/mg_{noble} in HER and 1.71 A/mg_{noble} in OER, which is approximately 10 times that of Pt/C for HER and 35 times that of Ir/C for OER.

The overall water splitting test in acidic electrolyte is performed with result shown in Fig. 3h. In this test, the Pt/C and Ir/C act as counter electrode and working electrode respectively. With the comparison of LSV, the Ir/Co Pt Pd@MX‖Ir/Co Pt Pd@MX achieves a cell voltage of 1.46 V while the commercial electrocatalyst shows 1.84 V. In terms of water splitting stability, the Ir/Co Pt@MX was used as a comparison due to its comparable OER and HER performances to Ir/Co Pt Pd@MX. As is shown in Fig. 3i, however, without the incorporation of Pd, the cell potential rapidly increases after 7 h, highlighting the limitations of electrocatalyst stability in acidic conditions. In contrast, the Ir/Co Pt Pd@MX maintains steady water splitting performance. Furthermore, the post reaction obser-

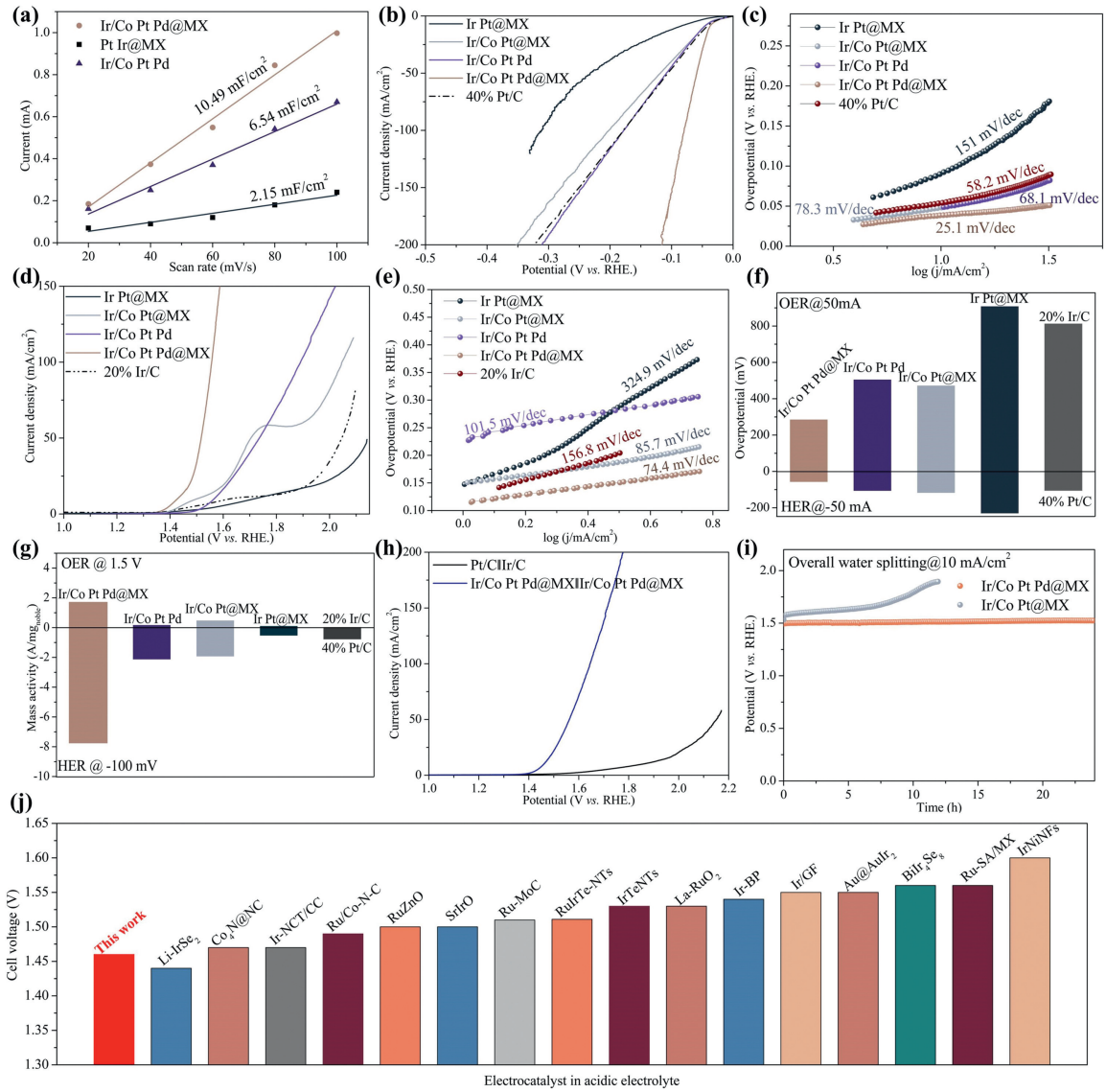


Fig. 3. (a) Double layer capacitance (C_{dl}) of Ir Pt@MX, Ir/Co Pt Pd and Ir/Co Pt Pd@MX, (b) HER linear scan voltammetry (LSV) of corresponded electrocatalysts, (c) Tafel slope of HER, (d) OER LSV of corresponded electrocatalysts, (e) Tafel slope of OER. (f) Bar chart of overpotential at 50 mA for OER and −50 mA for HER of each electrocatalyst, (g) bar chart of mass activity normalized to per milligram noble metal of 1.5 V for OER and −100 mV for HER. (h) LSV for overall water splitting in acidic electrolyte of Ir/Co Pt Pd@MX and commercial Pt/C and Ir/C electrode. (i) Stability test at 10 mA in overall water splitting of Ir/Co Pt Pd@MX and Ir/Co Pt@MX. (j) Comparison of overpotential at 10 mA/cm^2 of state-of-art electrocatalysts in acidic water splitting [6–8,40–52].

vation of HRTEM of Ir/Co Pt Pd@MX in Fig. S16 (Supporting information) still shows the crystal lattice of PdO, IrO_2 and PtO, indicating no overoxidation of IrO_2 happened. Fig. 3j compares state-of-the-art acidic water splitting electrocatalysts, illustrating that the 1.46 V cell voltage achieved by Ir/Co Pt Pd@MX is among the best compared to other noble-metal based electrocatalysts. A detailed comparison of the corresponding works is provided in Table S1 (Supporting information).

A series of DFT calculation is performed to investigate the kinetics of Ir/Co Pt Pd@MX in overall water splitting. Firstly, the affection of Co in synthesis process is being revealed by the Gibbs free energy calculation of Ir deposition. As is shown in Fig. 4a, the deposition energy of Ir on the surface of IrO_2 changed from −3.26 eV with no Co introduced to −3.93 eV as the introduction of Co. This indicates the Co helps with the deposition of Ir in the electrocatalyst. The easier for deposition of Ir, the more adequate usage of Ir-based catalyst. As for the Pd role as a protector, Fig. 4b shows the Gibbs free energy calculation of H* absorption on Ir site. With Pd be introduced as “proton acceptor”, the energy change from −0.31 eV to −0.41 eV, showing 33 % changing rate. Obviously, with Ir site being tough to absorb H^+, the negative affection of acidic environment to Ir site is limited, which is beneficial for Ir active site in long term stability in water splitting.

Since the effects of Co and Pd are displayed in both experimental and theoretical ways. The Gibbs free energy calculations of HER and OER are performed. For the HER, the Pt and PtO are taken as references. The three noble metal active sites are all taken into consideration as is shown in Fig. 4c. The free energy calculation results are shown in Fig. 4d Since the Pd limit the absorption of H^+ on Ir site. The Ir site shows poorer HER activity than both Pt and Pd. But all three sites are still better than Pt (−0.15 eV) and PtO (−0.18 eV), where the Pt acting as primary site out performs all active site with lowest Gibbs free energy in HER (−0.11 V). Both free energy calculation of OER at 0 V and 1.23 V are performed while the atomic configurations are shown in Fig. S17 (Supporting information). The transition from *O to *OOH is usually considered

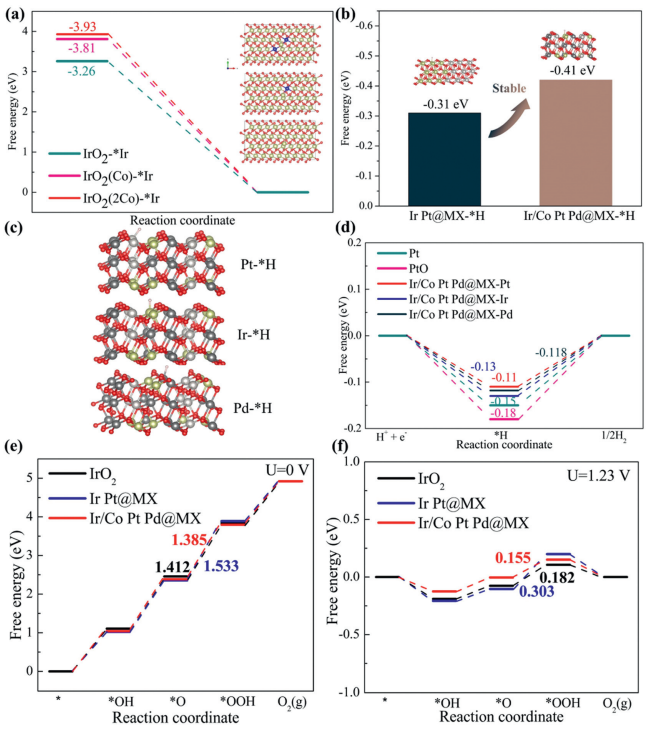


Fig. 4. (a) Gibbs free energy of Ir deposition on IrO_2 with the addition of Co. (b) H^* absorption free energy of Ir Pt@MX and Ir/Co Pt Pd@MX. (c) Atomic configuration of $^*H$ absorption on Ir/Co Pt Pd@MX on difference active sites. (d) HER free energy calculation of corresponding samples. OER free energy calculation of corresponding samples under (e) $U = 0$ V and (f) $U = 1.23$ V.

as the rate-determining step (RDS) for OER [56]. Ir/Co Pt Pd@MX shows the lowest free energy in RDS. While IrO_2 is taken as references, Ir Pt@MX shows poorer OER performance based on RDS calculation in Fig. 4e. This is because the simple combination of Ir and Pt is not competitive to commercial IrO_2. Furthermore, the deposition of Pt, which is not favored for OER, occupying active site for Ir. While for Ir/Co Pt Pd@MX, the introduction of Pd, part of the triple metal oxides, helps with OER, leading to a lower free energy in RDS. Same phenomenon is also shown in Fig. 4f, where the Ir/Co Pt Pd@MX shows lower free energy of RDS (0.155 eV) than IrO_2 (0.182 eV).

In summary, a noble metal-based electrocatalyst suitable for use in acidic electrolytes has been successfully synthesized, featuring Pt/Ir as active sites and Pd as a "H^+ acceptor." The introduction of Co during synthesis results in increased valence states for both Pt and Ir, as confirmed by XPS spectra and EXAFS analysis, thereby enhancing overall water splitting performance. The use of MXene sheets as a substrate further increases the ECSA of the Ir/Co Pt Pd@MX catalyst. This electrocatalyst exhibits a low HER overpotential of 38 mV at -10 mA/cm^2 and a low Tafel slope of 25.1 mV/dec, both outperforming the commercial Pt/C electrocatalyst. Similarly, the OER performance shows an overpotential of 230 mV at 10 mA/cm^2 and a Tafel slope of 74.4 mV/dec. Additionally, the overall water splitting demonstrates a low cell voltage of 1.46 V, with the stability of Ir/Co Pt Pd@MX showing almost no decay after 24 h, whereas the Pd-free variant loses efficiency rapidly after 7 h. DFT calculations reveal that Co facilitates the deposition of Ir, while Pd prevents H^* absorption by Ir, protecting the Ir during long-term acidic testing. The RDS for both HER and OER are effectively reduced compared to Pt and PtO in HER and IrO_2 in OER. This study provides a novel strategy for the development of noble metal-based electrocatalysts for acidic overall water splitting.

Declaration of competing interest

The authors declare that they have no known competing financial interests or personal relationships that could have appeared to influence the work reported in this paper.

CRediT authorship contribution statement

Zicong Yang: Writing – original draft, Methodology, Investigation, Formal analysis, Conceptualization. **Guangshun Ran:** Software, Investigation, Data curation. **Hui Song:** Methodology, Data curation. **Yukun Chang:** Investigation, Formal analysis, Data curation. **Jinshu Wang:** Resources, Project administration. **Hongyi Li:** Writing – review & editing, Supervision, Project administration, Funding acquisition, Conceptualization.

Acknowledgments

A portion of this work is based on the data obtained at BSRF-1W2B beamline. This work was financially supported by Beijing Municipal Commission of Education (No. KZ202210005003), Beijing Natural Science Foundation (No. Z210016), National Key Research and Development Program of China (No. 2022YFB3705403).

Supplementary materials

Supplementary material associated with this article can be found, in the online version, at doi:10.1016/j.cclet.2025.111370.

References

[1] L. Quan, H. Jiang, G. Mei, Y. Sun, B. You, Chem. Rev. 124 (2024) 3694–3812.
[2] G.K. Kiran, T.V. Sreekanth, K. Yoo, et al., Mater. Chem. Phys. 296 (2023) 127272.
[3] T. Rasheed, A. Rasheed, F.M. Alzahrani, et al., Fuel 346 (2023) 128305.
[4] J. Wang, H. Yang, F. Li, et al., Sci. Adv. 8 (2022) eabl9271.
[5] S.S. Kumar, S.U. Ramakrishna, B. Rama Devi, et al., Ionics 24 (2018) 3113–3121.
[6] J. Zhang, G. Wang, Z. Liao, et al., Nano Energy 40 (2017) 27–33.
[7] C. Rong, X. Shen, Y. Wang, et al., Adv. Mater. 34 (2022) e2110103.
[8] Z. Wang, P. Wang, H. Zhang, et al., J. Mater. Chem. A 9 (2021) 18576–18581.
[9] X. Wang, J. Hu, T. Lu, et al., Angew. Chem. Int. Ed. 64 (2024) e202415306.
[10] P. Jovanovic, N. Hodnik, F. Ruiz-Zepeda, et al., J. Am. Chem. Soc. 139 (2017) 12837–12846.
[11] X. Wang, Z. Qin, J. Qian, et al., ACS Catal. 13 (2023) 10672–10682.
[12] L. Chong, J. Wen, E. Song, et al., Adv. Energy Mater. 13 (2023) 2302306.
[13] Q. Dang, H. Lin, Z. Fan, et al., Nat. Commun. 12 (2021) 6007.
[14] X. Bao, S. Li, C. Hao, et al., J. Mater. Chem. A 10 (2022) 20005–20010.
[15] P. Wang, X. Wu, M. Li, et al., J. Rare Earths (2024), doi:10.1016/j.jre.2024.11.001.
[16] M. Li, X. Wang, K. Liu, et al., Adv. Energy Mater. 13 (2023) 2301162.
[17] Y. Chang, Y. Chen, Z. Yang, et al., J. Alloy. Compd. 968 (2023) 171859.
[18] Y. Wang, L. Zhang, K. Yin, et al., ACS Appl. Mater. Interfaces 11 (2019) 39728–39736.
[19] M. Naguib, M. Kurtoglu, V. Presser, et al., Adv. Mater. 23 (2011) 4248–4253.
[20] B. Anasori, M.R. Lukatskaya, Y. Gogotsi, et al., Nat. Rev. Mater. 2 (2017) 16098.
[21] G. Gao, A.P. O'Mullane, A. Du, et al., ACS Catal. 7 (2016) 494–500.
[22] M. Naguib, V.N. Mochalin, M.W. Barsoum, et al., Adv. Mater. 26 (2014) 992–1005.
[23] M. Zubair, M.M. Ul Hassan, M.T. Mehran, et al., Int. J. Hydrogen Energ. 47 (2022) 2794–2818.
[24] Y. Yuan, H. Li, L. Wang, et al., ACS Sustain. Chem. Eng. 7 (2019) 4266–4273.
[25] K. Zhao, X. Ma, S. Lin, et al., ChemistrySelect 5 (2020) 1890–1895.
[26] F. Ming, H. Liang, G. Huang, et al., Adv. Mater. 33 (2021) e2004039.
[27] A. Jayakumar, R.P. Antony, R. Wang, et al., Small 13 (2017) 1603102.
[28] R. Ma, Z. Chen, D. Zhao, et al., J. Mater. Chem. A 9 (2021) 11501–11529.
[29] Z. Yang, Y. Chen, G. Chen, et al., Heliyon 9 (2023) e19197.
[30] P. Strasser, Acc. Chem. Res. 49 (2016) 2658–2668.
[31] J. Quinson, M. Inaba, S. Neumann, et al., ACS Catal. 8 (2018) 6627–6635.
[32] B. Jiang, Y. Guo, J. Kim, et al., J. Am. Chem. Soc. 140 (2018) 12434–12441.
[33] C.F. Linsey, C. Seitz, K. Nishio, et al., Science 353 (2016) 4.
[34] S.K. Ailong Li, K. Adachi, H. Ooka, et al., Science 384 (2024) 666.
[35] M.Y. Fan, J.J. Wang, J. Zhao, et al., Rare Metals 43 (2024) 1537–1546.
[36] T. Li, L. Yao, Q. Liu, et al., Angew. Chem. Int. Ed. 57 (2018) 6115–6119.
[37] L. Huang, T. Li, Q. Liu, et al., Electrochem.Commun. 104 (2019) 106472.
[38] B. Liu, Y. Wang, H.Q. Peng, et al., Adv. Mater. 30 (2018) e1803144.
[39] Q. Wang, C.Q. Xu, W. Liu, et al., Nat. Commun. 11 (2020) 4246.
[40] D. Zhang, C. Sun, D. Liu, et al., Sci. China Mater. 66 (2023) 1362–1372.
[41] C. Yang, X. Zhang, Q. An, et al., J. Energy Chem. 78 (2023) 374–380.
[42] Z. Liu, Y. Liu, H. He, et al., Electrochim. Acta 443 (2023) 141920.

[43] L. Hou, Z. Li, H. Jang, et al., Adv. Energy Mater. 13 (2023) 2300177.
[44] Y. Wu, R. Yao, Q. Zhao, et al., Chem. Eng. J. 439 (2022) 135699.
[45] L. Zhang, H. Jang, Z. Li, et al., Chem. Eng. J. 419 (2021) 129604.
[46] X. Wang, D. Wang, W.J. Yin, et al., Adv. Energ. Sust. Res. 2 (2021) 2000074.
[47] H. Wang, Z.N. Chen, D. Wu, et al., J. Am. Chem. Soc. 143 (2021) 4639–4645.
[48] X. Peng, S. Zhao, Y. Mi, et al., Small 16 (2020) e2002888.
[49] T. Zheng, C. Shang, Z. He, et al., Angew. Chem. Int. Ed. 58 (2019) 14764–14769.
[50] F. Lv, W. Zhang, W. Yang, et al., Small Methods 4 (2019) 1900129.
[51] J. Mei, T. He, J. Bai, et al., Adv. Mater. 33 (2021) e2104638.
[52] M. Liu, S. Liu, Q. Mao, et al., J. Mater. Chem. A 10 (2022) 2021–2026.
[53] L. Meng, L.K. Yan, F. Viñes, et al., J. Mater. Chem. A 11 (2023) 6886–6900.
[54] Y. Tang, C. Yang, Y. Yang, et al., Electrochim. Acta 296 (2019) 762–770.
[55] F. Luo, S. Pan, Y. Xie, et al., Adv. Sci. 10 (2023) e2305058.
[56] A. Grimaud, A. Demortière, M. Saubanère, et al., Nat. Energy 2 (2016) 16189.